CHINESE OPTICS LETTERS

Vol. 23, No. 12 | December 2025

Evolution of circularly polarized states spawned from off-Γ point BICs

Chang Liu (刘 畅)[1,†], Zhongxia Du (杜中霞)[1,†], Shanhe Pang (庞善核)[1], Miaoqing Yang (杨苗青)[1], Yanyong Li (李炎勇)[1], Jun Wang (王 俊)[1*], Jiajun Wang (王佳俊)[2**], and Bo Wang (王 博)[1,3***]

[1] Henan Key Laboratory of Quantum Materials and Quantum Energy, School of Quantum Information Future Technology, Henan University, Zhengzhou 450046, China

[2] State Key Laboratory of Surface Physics, Key Laboratory of Micro- and Nano-Photonic Structures (Ministry of Education) and Department of Physics, Fudan University, Shanghai 200433, China

[3] Institute of Quantum Materials and Physics, Henan Academy of Sciences, Zhengzhou 450046, China

[†]These authors contributed equally to this work.

*Corresponding author: junwang2024@henu.edu.cn

**Corresponding author: jiajunwang@fudan.edu.cn

***Corresponding author: bowang@henu.edu.cn

Received May 23, 2025 | Accepted August 5, 2025 | Posted Online November 6, 2025

Bound states in the continuum (BICs) can manifest as vortex polarization singularities in momentum space. The BICs at Γ point are proved to be protected by the rotational symmetry, and previous studies have explored the at-Γ BICs split into pairs of circularly polarized states with opposite chirality after breaking the in-plane inversion symmetry. As another type of conventional BICs, off-Γ BICs, have been less explored in their evolution and modulation relations compared to their at-Γ counterparts. Here, we investigate the evolution of circularly polarized states spawned from off-Γ BICs by selectively breaking in-plane and out-of-plane symmetry. The circularly polarized states exhibit distinct evolutionary trajectories under different symmetry-breaking conditions. This study offers an effective approach for manipulating the evolution of circularly polarized states in momentum space from off-Γ BICs, holding promise for potential applications in the field of polarization modulation and topological photonics.

Keywords: bound states in the continuum; circularly polarized states; symmetry breaking.
DOI: 10.3788/COL202523.123604

1. Introduction

Bound states in the continuum (BICs) are non-radiative, spatially localized states that exist within the continuous radiation spectrum[1,2]. They manifest as non-radiative optical modes, with theoretically infinite lifetimes, confined within photonic crystal (PhC) slabs[3–7] or other structures[8–10]. In PhC slabs, BICs are exhibited as centers of polarization vortices in momentum space, carrying integer topological charges[11–13]. These unique topological properties of BICs hold prospective applications in advanced photonic technologies such as lasers[14–16] and sensors[17–20]. So far, most BICs have been demonstrated in mirror-symmetric structures. When the symmetry of the structure is broken, a BIC is decomposed into a pair of circularly polarized points (*C* points) with opposite chirality[21–26]. This symmetry breaking initiates a remarkable evolution in the behavior and characteristics of the BIC, and the ability to manipulate *C* points spawned from BICs provides new possibilities for controlling optical fields and light detection[27–33].

BICs occur throughout momentum space, at both Γ points and off-Γ points[11,24,34,35]. Most current research is concentrated on the evolutionary behavior of BICs at Γ points following symmetry breaking[29,36–40]; at-Γ BICs are protected by rotational symmetry and remain at the Γ point until the symmetry is broken. In contrast, off-Γ BICs originate from coherent cancellation of upward and downward radiative channels[35], and breaking mirror or inversion symmetry disrupts this interference condition, causing the off-Γ BIC to evolve into a pair of *C* points carrying half-integer topological charges[36,41]. This distinction makes off-Γ BICs a promising platform to explore richer mechanisms of *C* point generation and control. At present, the evolutionary behavior of BICs at off-Γ points is rarely reported. Here, separately breaking in-plane inversion (C_2) and out-of-plane mirror (σ_z) symmetries of PhC slabs, we investigate the evolution of *C* points spawning from off-Γ BICs. We vary each asymmetry parameter in turn and show the corresponding *C* point trajectories. The results indicate that

different types of symmetry breaking produce distinct C point trajectories. This provides a new approach for manipulating C points: through specific symmetry breaking, they can be moved to any position in momentum space. This also presents potential applications in fields such as light manipulation and singular optics.

2. Results and Discussion

First, we simulate a BIC at an off-Γ point using the finite-element method. We consider two-dimensional PhC slabs [see Fig. 1(a)], in which a square lattice (periodicity $a = 450$ nm) of square air holes ($L = 247$ nm) is patterned in silicon nitride ($n = 2.02$, $S_0 = L^2$ common in the laboratory). The 200 nm thick slab, with no substrate, maintains its up-down mirror symmetry. All modes in this system can be classified as TE-like or TM-like. TE-like and TM-like modes are derived from the conventional definitions of transverse electric and transverse magnetic modes. In photonic crystal slabs, due to the lack of continuous translational symmetry along the z-direction, the modes are not strictly TE or TM. Instead, we use the symmetry of the electric and magnetic fields at the mid-plane of the slab to categorize the entire band as TE-like or TM-like. Here, we focus on the TM_2 band and numerically simulate a BIC at an off-Γ point. The band structure and quality factor (Q factor) are shown in Fig. 1(b), in which the TM_2 band is indicated with a red line and its Q factor is indicated in blue. A BIC is found along the k_x-axis, off the normal direction at $k_x a/(2\pi) = 0.385$. Figure 1(c) plots the Q factor near this BIC in momentum space, showing how it tends to diverge.

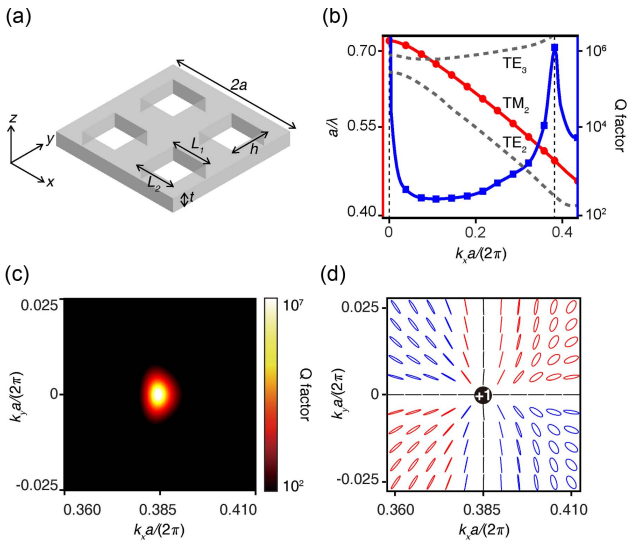

Fig. 1. Observation of off-Γ BICs. (a) Schematic of the two-dimensional PhC slabs. (b) Band structures along the Γ-X direction. The TM_2 band is indicated by the red line, and its Q factor is represented by the blue line. (c) Variation of the Q factor in momentum space near the BIC. (d) Far-field polarization maps in the vicinity of the off-Γ point, where the red (blue) ellipse indicates the left (right)-handed polarized state, and the black line corresponds to the linearly polarized state.

The polarization maps for far-field radiation near the BIC are plotted in Fig. 1(d). We define the topological charge as the winding number of the polarization major axis around the BIC in momentum space. This vortex exhibits a positive topological charge.

2.1. In-plane symmetry breaking

To analyze in depth the evolution of C points following the disruption of a BIC, and to quantitatively assess the degree of structural symmetry variation, we implemented a continuous modulation scheme for symmetry breaking. Throughout this process, the total area of the unit cell was kept constant to ensure overall structural stability.

Initial parameters obtained from the design specifications were input to construct the PhC slabs structure model. To quantitatively characterize the degree of in-plane symmetry breaking, we introduce the symmetry-breaking parameter α, as shown in Fig. 2(a):

$$L_3 = \sqrt{2S_0/(2-\alpha)}, \tag{1}$$

$$L_1 = (1-\alpha)L_3. \tag{2}$$

We used these equations to reverse-calculate the scaling of the top and bottom edge lengths (L_1 and L_3) of the air slots in the PhC slabs as the parameter α, which governs the scaling process, varying from zero to one, thereby achieving in-plane symmetry breaking. We used COMSOL finite element analysis to obtain electric field data (E_x, E_y) for different values of α. This revealed the impact of mirror symmetry breaking on the splitting of BICs and the evolution of C point displacement.

To better observe the pair of C points with opposite chirality, we use the polarization orientation angle[41,42]:

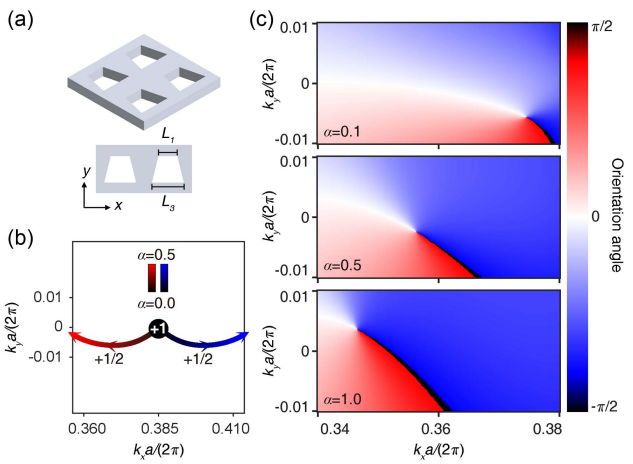

Fig. 2. Schematic of in-plane inversion (C_2) symmetry breaking by variation of α. (a) Schematic of the PhC slabs with an isosceles trapezoidal in-plane shape. (b) Evolution in momentum space of the pair of C points generated by the splitting of the BIC as the edge lengths change. Blue (red) indicates right (left) circular polarization. (c) Distribution of the far-field radiation polarization orientation angle ϕ in momentum space for α = 0.1, 0.5, and 1.0.

$$\phi = \frac{1}{2}\arg(S_1 + iS_2). \tag{3}$$

This quantifies the orientation of the major axis of the far-field polarization ellipse to the x-axis, providing a quantitative method for analyzing the topological properties of polarization singularities in momentum space. The procedure reveals the local topological features of these singularities and facilitates the mapping of the polarization state distribution across the entire Brillouin zone. This offers an intuitive visualization of the topological structure of polarization states in momentum space.

We obtained images at each incremental step of this process. In Fig. 2(b), after establishing a definitive method to confirm the positions of the C points, we quantified the displacement trajectories corresponding to variations in the symmetry-breaking parameter α. The results reveal systematic trajectories in momentum space of C points that have split from the off-Γ BIC. Besides, we also plotted the trajectory of the polarization states at a specific wavevector on the Poincaré sphere; see more details in the Supplement 1. The disruption of in-plane inversion symmetry causes a pronounced separation of the C points along the k_x-direction, in contrast to the predominantly k_y-direction displacement observed under out-of-plane symmetry breaking; detailed comparisons will be shown in the next section. As α gradually increases, this pair of C points progressively diverges along the k_x-axis and becomes symmetrically distributed on both sides of the original off-Γ BIC position. Their trajectories clearly demonstrate the effect of variations in structural symmetry parameters on the modulation of polarization states.

In Fig. 2(c), the left-handed C point was tracked, and the distribution of angle ϕ was analyzed to further examine the effects of in-plane symmetry breaking. When α is low (e.g., $\alpha = 0.1$), the pair of C points has just separated from the BIC, and the ϕ distribution is approximately symmetric, indicating a relatively small perturbation. As α increases to 0.5, the left-handed and right-handed C points begin to separate, with both points starting to move along the k_x-direction. When α reaches 1.0, the far-field polarization map exhibits a pronounced shift, and distinct boundaries emerge between different regions. The areas corresponding to the black and white regions increase, and the two C points become completely separated. This indicates that the anisotropic scaling of the top and bottom lengths (L_1 and L_3) results in structural deformation, leading to a redistribution of the far-field polarization states and a migration of the polarization singularities in momentum space. It also demonstrates that as the degree of symmetry breaking increases, the disruption of the BIC becomes increasingly intense.

Using Eq. (3), we employed an interpolation algorithm to finely fit electric field data obtained from our simulations, thereby enhancing the resolution. This enabled us to extract precise coordinates of the boundaries of the polarization orientation regions. This approach refines the field distribution and enables more precise determination of C point positions by identifying the crossings of the polarization orientation angle. The interpolation does not alter the underlying physical data but improves the numerical accuracy within the limits of the FEM mesh. We verified that the C point positions converge upon further refining the original simulation grid, confirming the robustness and reliability of the interpolation-based analysis. This is shown in Fig. 2(c), where black regions correspond to polarization angles perpendicular to the x-axis, white regions indicate angles parallel to the x-axis, red denotes polarization ellipse major axis angles in the first and third quadrants, and blue represents angles in the second and fourth quadrants. These boundary coordinates correspond precisely to the positions of the C points.

This interpolation-based analysis addresses the problem of blurring of circular polarization points caused by large simulation step sizes. It also provides a reliable means to record and track the evolution of these points in momentum space with high precision. By systematically varying the symmetry-breaking parameters, we investigated precisely how the circular polarization points shift and reorganize in momentum space as the structural symmetry is altered.

2.2. Out-of-plane symmetry breaking

In this section, we examine the effects of breaking the out-of-plane mirror (σ_z) symmetry of the model representing the PhC slabs structure. Based on the characteristics of the crystal structure along the σ_z direction, we employed four distinct symmetry-breaking strategies: breaking along the x-direction, y-direction, x- and y-directions simultaneously; and altering the substrate refractive index.

Under each of these symmetry-breaking conditions, we systematically investigated the evolution of C points carrying half-integer topological charges generated from the splitting of off-Γ BICs. By adjusting parameters, we achieved fine control over the splitting process of the BICs and the subsequent trajectories of the C points. This also enabled us to isolate and control the impact of out-of-plane symmetry breaking on BICs and their derived circularly polarized singularities without affecting the in-plane symmetry.

2.2.1. Symmetry broken by the x-direction

To break the mirror symmetry along the z-direction in the PhC slabs while ensuring that air was present on both the top and bottom surfaces, so that the refractive index remained constant, we tilted the walls of the air holes. This was implemented by adjusting the upline (L_1) and baseline (L_2) edge lengths of the air hole sidewalls along the x-direction, keeping the lateral area constant to preserve the duty cycle. A tunable parameter β was introduced to quantify the degree of structural asymmetry, according to the equations below. As the value of β increases, the mirror symmetry between the top and bottom parts of the slab is progressively altered, as illustrated in Fig. 3(a):

$$L_2 = \sqrt{2S_0/(2-\beta)}, \tag{4}$$

$$L_1 = (1-\beta)L_2. \tag{5}$$

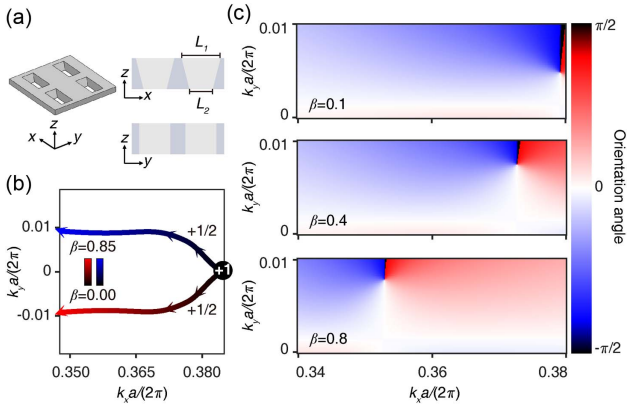

Fig. 3. Disruption of structural symmetry along the *z*-direction through variation of the upline (L_1) and baseline (L_2) edge lengths in the *x*-direction. (a) Schematic of the PhC slabs with trapezoidal sidewalls in the *x*-direction. (b) Evolution in momentum space of the pair of *C* points generated by the splitting of the BIC as the edge lengths change. Blue (red) indicates right-handed (left-handed) circular polarization. (c) Distribution of the far-field radiation polarization orientation angle ϕ in momentum space for $\beta = 0.1$, 0.4, and 0.8.

Figure 3(b) illustrates the evolution in momentum space of the circularly polarized singularities generated by the splitting of the off-Γ BIC as the asymmetry parameter β is gradually increased. For small β values, a pair of polarization singularities appears near the original BIC. As structural asymmetry intensifies, these singularities begin to split along the k_x-direction, while remaining symmetrically aligned along $k_y = 0$. This shows the effect of out-of-plane symmetry breaking on the polarization state: with increasing β, the singularities' trajectories become more parallel. When β reaches 0.85, the interaction between the right-handed and left-handed *C* points weakens, the separation between the singularities attains its maximum, and their trajectories stabilize, demonstrating a marked reduction in the coupling between oppositely handed states.

Figure 3(c) displays the distributions of far-field radiation polarization orientation angles in momentum space for three representative β values: 0.1, 0.4, and 0.8. At $\beta = 0.1$, the angles are distributed symmetrically near $k_y = 0$, with localized regions showing opposite symmetry in the off-Γ area. As β increases to 0.4, the singularity regions become more extensive and shift further away, exhibiting larger steps along the k_y-direction. At $\beta = 0.8$, the polarization states undergo significant reorganization, with the regions corresponding to circular polarization predominantly extending along the k_x-axis.

2.2.2. Symmetry broken by the *y*-direction

To further investigate the influence of *z*-direction symmetry breaking on the evolution of far-field polarization states, we tilted the air-hole walls along the *y*-direction in the PhC slabs. This was done while ensuring both upline (L_1) and baseline (L_2) lengths of the trapezoidal surfaces remained in contact with air, so the refractive index remained constant. The same mathematical framework was used for *x*-direction compression, proportionally modifying the dimensions of the trapezoidal air slot upline (L_1) and baseline (L_2) edge lengths using the same relationship as that for the *x*-direction, to characterize the degree of compression along the *y*-direction. As the value of β gradually increases, the mirror symmetry between the upline (L_1) and baseline (L_2) lengths of the trapezoidal parts of the slab is increasingly broken, as shown in Fig. 4(a).

Figure 4(b) presents the evolution trajectory in momentum space of the pair of *C* points generated by the splitting of the BIC during the edge length adjustment process. Notably, compared to the primarily k_x-direction displacement observed under *x*-direction compression, this out-of-plane symmetry breaking causes a more pronounced displacement of the *C* points along the k_y-axis. Initially, when β is small, the pair of circularly polarized states exhibits only slight displacement along both the k_x- and k_y-axes. However, as β increases, the displacement becomes progressively larger, with a greater shift along the k_y-direction. When β approaches its maximum value, the separation between the two *C* points almost reaches its maximum and their trajectories become stabilized.

Figure 4(c) details the distribution of the far-field radiation polarization orientation angle ϕ in momentum space for β values of 0.1, 0.4, and 0.8. For smaller β values, the *C* points are concentrated near $k_y = 0$, indicating that the oppositely handed pair of polarization singularities has only just begun to split. As β increases to 0.4, the spiral regions (displayed in red, white, blue, and black) clearly expand along the k_y-direction, demonstrating that the orientation of the polarization ellipse's major axis

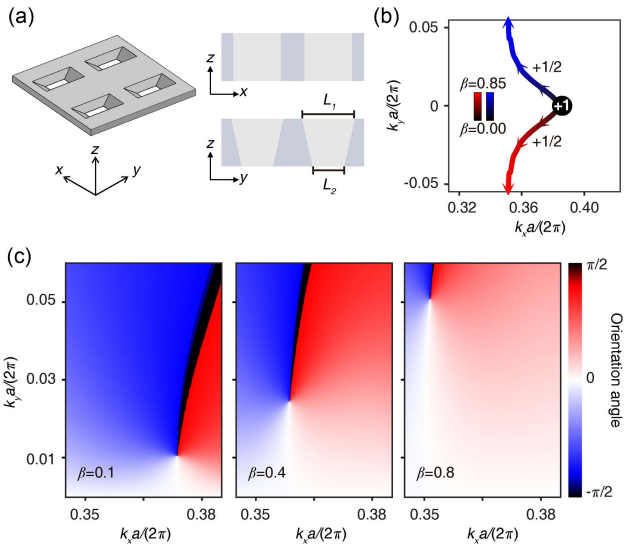

Fig. 4. Disruption of structural symmetry along the *z*-direction through variation of the upline and baseline edge lengths along the *y*-direction. (a) Schematic of the PhC slabs with trapezoidal sidewalls in the *y*-direction. (b) Evolution in momentum space of the pair of circularly polarized points generated by the splitting of the BIC as the edge lengths change. (c) Distribution of the far-field radiation polarization orientation angle ϕ in momentum space for β = 0.1, 0.4, and 0.8.

transitions from being locally concentrated to more dispersed. When β reaches 0.8, the polarization singularities shift to a position close to $k_y a/(2\pi) = 0.05$, indicating that the C points have significantly separated along the k_y-direction.

These results show that under the condition that in-plane symmetry is maintained, precise control of out-of-plane asymmetry—achieved by tilting the sidewalls in the y-direction—enables accurate positioning and manipulation of C points in momentum space.

2.2.3. Symmetry broken by both the *x*-direction and the *y*-direction

To rigorously validate the correlation between the evolution of C points and the Γ-X direction in the PhC slabs, we adjusted the lateral wall lengths along the x- and y-directions simultaneously. This transformed each original air trench into an inverted truncated quadrilateral pyramid structure measured by geometric parameter β. This structural modification introduces an additional hierarchy of asymmetry, thereby more thoroughly disrupting the out-of-plane mirror symmetry along the z-direction. Under such intricate symmetry broken conditions, we systematically investigated the behavior of circularly polarized states in momentum space.

Figure 5 illustrates the structural evolution and its effects. Figure 5(a) depicts a representative model with symmetrically truncated sidewalls. Figure 5(b) shows how an incremental increase of the asymmetry parameter β drives the transition of the inverted truncated pyramid toward a standard inverted quadrangular pyramid. This amplifies symmetry breaking, resulting in pronounced displacement in momentum space of circularly polarized singularities originating from BICs. Observations show that the displacement magnitude along the k_y-direction significantly exceeds that along k_x with increasing β, strongly supporting the theoretical linkage between circular polarization dynamics and Γ-X directional symmetry-breaking mechanisms.

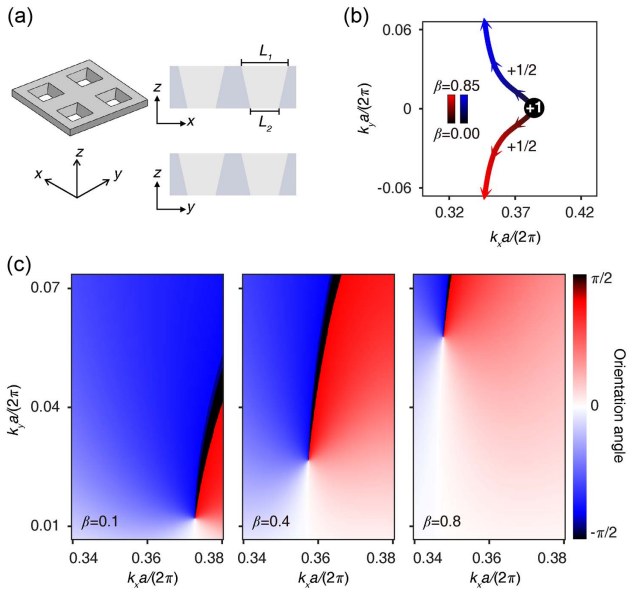

Fig. 5. Disruption of structural symmetry along the z-direction through variation of the upline and baseline edge lengths along both x- and y-directions. (a) Schematic of the PhC slabs with trapezoidal sidewalls in both the x- and y-directions. (b) Evolution in momentum space of the pair of C points generated by the splitting of the BIC as the edge lengths change. (c) Distribution of the far-field radiation polarization orientation angle ϕ in momentum space for β = 0.1, 0.4, and 0.8.

Figure 5(c) further analyzes the momentum-space distribution of far-field radiation polarization orientation angles for β values of 0.1, 0.4, and 0.8. At $\beta = 0.1$, the angles predominantly cluster near $k_y = 0$, with residual linear polarization components (white/black regions) persisting near the original off-Γ BIC positions. As β increases to 0.4 and 0.8, the black and white regions progressively collapse into linear features, while red-dominated regions expand, signifying a substantial redistribution of far-field polarization. Circularly polarized states exhibit a distinct displacement trend along the k_y-axis, corroborating the role of asymmetric geometry in governing polarization evolution.

These results demonstrate that simultaneous adjustment of the upline and baseline edge lengths of air trench sidewalls along the x- and y-directions effectively disrupts out-of-plane mirror symmetry, enabling precise generation, separation, and stabilization of circularly polarized states in momentum space. The engineered asymmetry not only induces measurable displacement of polarization singularities but also induces far-field polarization variation.

2.2.4. Refractive index modification

As another means of disrupting the out-of-plane mirror symmetry (σ_z) of the PhC slabs, we introduced, above the slab, an infinitely thick substrate with a different refractive index. As illustrated in Figs. 6(a) and 6(b), when the substrate refractive index n_{sub} increases progressively from 1.0 to 1.6, off-Γ BICs undergo splitting, generating pairs of circularly polarized states with opposite handedness. This transformation decomposes the original BIC with integer topological charge into two polarization singularities carrying half-integer topological charges ($+1/2$ and $-1/2$).

Figure 6(c) displays the polarization orientation angle distribution, revealing that the circularly polarized states with opposite chirality exhibit symmetric evolution trajectories along $k_y = 0$ in momentum space. As n_{sub} increases, the deviation of these topological singularities becomes more pronounced. For low n_{sub}, the opposite chirality C points tend to converge symmetrically toward the Γ-point, indicating strong mutual coupling. For higher n_{sub}, this coupling weakens, leading to repulsive interactions that drive the polarization states apart in momentum space. Such displacement highlights the critical role of the substrate in modulating photonic band structures—particularly in altering far-field symmetry—and underscores the profound influence of substrate refractive index on the generation, interaction, and separation of topological singularities.

Polarization orientation angle maps confirm that increasing n_{sub} induces significant far-field polarization redistribution. The

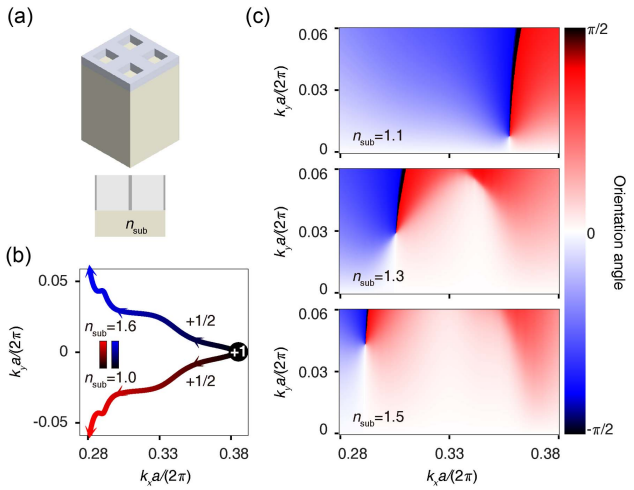

Fig. 6. Breaking structural symmetry along the *z*-direction by varying substrate refractive index. (a) Schematic of the PhC slabs with substrate above. (b) Evolution in momentum space of a pair of *C* points generated by the splitting of an off-Γ BIC as the substrate refractive index increases. (c) Distribution of far-field radiation polarization orientation angle ϕ in momentum space for n_{sub} = 1.1, 1.3, and 1.5.

orientation angles of polarization ellipses become larger, and the spatial extents of regions with opposite chirality progressively expand, demonstrating the broad impact of substrate-induced symmetry breaking on far-field polarization characteristics. Thus, by engineering the substrate refractive index, we can control the generation and evolution of topological singularities in momentum space, enabling tailored manipulation of circularly polarized states.

3. Conclusion

We investigated the impact of breaking out-of-plane mirror (σ_z) symmetry and in-plane inversion (C_2) symmetry on the polarization characteristics of PhC slabs. We demonstrated the ability to regulate the evolutionary trajectory and trends of circularly polarized points generated at off-Γ positions through symmetry-breaking mechanisms. These mechanisms not only disrupt the non-radiative vortex singularities associated with off-Γ BICs but also lead to the emergence of polarization singularities, or circularly polarized states, in their vicinity. These circularly polarized states exhibit distinct polarization structures, which evolve dynamically in momentum space as the symmetry-breaking parameters are varied.

We demonstrated the generation and evolutionary trajectories of these circularly polarized states under the influence of structural asymmetry. We used four different methods of breaking out-of-plane symmetry: by varying the structure in the *x*- and *y*- directions separately and combined, and by adding a substrate above the slab. Our findings provide robust theoretical and numerical support for controlled generation and regulation of polarization singularities, and offer valuable possibilities for applications in polarization control and topological photonics.

Breaking σ_z symmetry induces anisotropic displacements of circularly polarized states along the k_y-axis, while breaking C_2 symmetry leads to splitting and divergence of polarization states along the k_x-axis. These contrasting behaviors underline the distinct effects of out-of-plane and in-plane symmetry breaking on the momentum-space polarization topology of PhC slabs. We mapped far-field polarization orientation angle distributions, revealing the redistribution and evolution of polarization states as the structural parameters are systematically modified. The results underscore the role of symmetry breaking in modulating the polarization topology of photonic systems.

This research advances our understanding of polarization singularities in momentum space for PhC slabs and connects with the broader field of topological photonics. The generation and manipulation of circularly polarized states provide a framework for exploring the range of behaviors of polarization singularities and their variations under symmetry-breaking mechanisms.

The ability to control and tailor polarization singularities in PhC slabs holds promise for a range of applications. These include polarization filtering, vector beam generation, and quantum optics, where precise control of polarization states is crucial. The demonstrated tunability of polarization structures in momentum space provides for future topological photonic systems, enabling the development of devices with advanced functionality. Such precise control of circularly polarized states and polarization singularities in momentum space can enable practical applications including polarization selective filters and beam splitters, on-chip generation of vector and vortex beams for optical communication and microscopy, as well as enhanced enantioselective sensing by tailoring the spatial distribution of chiral fields. These examples highlight the technological potential of our approach beyond the fundamental insights into symmetry-breaking phenomena. Our results highlight the potential of symmetry-breaking strategies to unlock novel optical properties in photonic structures, paving the way for transformative advances in photonics and optoelectronics.

Acknowledgements

This work was supported by the National Natural Science Foundation of China (No. 12522420) and the China Postdoctoral Science Foundation (Nos. 2023M741024 and 2024T170218). J. W. was further supported by the Science and Technology Commission of Shanghai Municipality (No. 24YF2702400).

References

1. H. Friedrich and D. Wintgen, "Interfering resonances and bound states in the continuum," Phys. Rev. A **32**, 3231 (1985).
2. J. Von Neumann and E. P. Wigner, "Über merkwürdige diskrete Eigenwerte," in *The Collected Works of Eugene Paul Wigner*, A. S. Wightman, ed. (Springer, 1993), p. 291.
3. C. W. Hsu, B. Zhen, J. Lee, *et al.*, "Observation of trapped light within the radiation continuum," Nature **499**, 188 (2013).

4. J. Lee, B. Zhen, S. Chua, *et al.*, "Observation and differentiation of unique high- Q optical resonances near zero wave vector in macroscopic photonic crystal slabs," Phys. Rev. Lett. **109**, 067401 (2012).
5. Y. Yang, C. Peng, Y. Liang, *et al.*, "Analytical perspective for bound states in the continuum in photonic crystal slabs," Phys. Rev. Lett. **113**, 037401 (2014).
6. R. Gansch, S. Kalchmair, P. Genevet, *et al.*, "Measurement of bound states in the continuum by a detector embedded in a photonic crystal," Light. Sci. Appl. **5**, e16147 (2016).
7. Y. Guo, M. Xiao, and S. Fan, "Topologically protected complete polarization conversion," Phys. Rev. Lett. **119**, 167401 (2017).
8. K. Koshelev, Y. Tang, K. Li, *et al.*, "Nonlinear metasurfaces governed by bound states in the continuum," ACS Photonics **6**, 1639 (2019).
9. L. Xu, K. Zangeneh Kamali, L. Huang, *et al.*, "Dynamic nonlinear image tuning through magnetic dipole Quasi-BIC ultrathin resonators," Adv. Sci. **6**, 1802119 (2019).
10. Y. Liang, K. Koshelev, F. Zhang, *et al.*, "Bound states in the continuum in anisotropic plasmonic metasurfaces," Nano Lett. **20**, 6351 (2020).
11. B. Zhen, C. W. Hsu, L. Lu, *et al.*, "Topological nature of optical bound states in the continuum," Phys. Rev. Lett. **113**, 257401 (2014).
12. Y. Zhang, A. Chen, W. Liu, *et al.*, "Observation of polarization vortices in momentum space," Phys. Rev. Lett. **120**, 186103 (2018).
13. H. M. Doeleman, F. Monticone, W. Den Hollander, *et al.*, "Experimental observation of a polarization vortex at an optical bound state in the continuum," Nat. Photonics **12**, 397 (2018).
14. A. Kodigala, T. Lepetit, Q. Gu, *et al.*, "Lasing action from photonic bound states in continuum," Nature **541**, 196 (2017).
15. C. Huang, C. Zhang, S. Xiao, *et al.*, "Ultrafast control of vortex microlasers," Science **367**, 1018 (2020).
16. M. Hwang, H. Lee, K. Kim, *et al.*, "Ultralow-threshold laser using super-bound states in the continuum," Nat. Commun. **12**, 4135 (2021).
17. F. Yesilkoy, E. R. Arvelo, Y. Jahani, *et al.*, "Ultrasensitive hyperspectral imaging and biodetection enabled by dielectric metasurfaces," Nat. Photonics **13**, 390 (2019).
18. A. Leitis, A. Tittl, M. Liu, *et al.*, "Angle-multiplexed all-dielectric metasurfaces for broadband molecular fingerprint retrieval," Sci. Adv. **5**, eaaw2871 (2019).
19. X. Gao, B. Zhen, M. Soljačić, *et al.*, "Bound states in the continuum in fiber Bragg gratings," ACS Photonics **6**, 2996 (2019).
20. J. Wang, X. Wang, Z. Wu, *et al.*, "Inherent spin-orbit locking in topological lasing via bound state in the continuum," Phys. Rev. Lett. **134**, 133802 (2025).
21. H. Zhou, C. Peng, Y. Yoon, *et al.*, "Observation of bulk fermi arc and polarization half charge from paired exceptional points," Science **359**, 1009 (2018).
22. W. Liu, B. Wang, Y. Zhang, *et al.*, "Circularly polarized states spawning from bound states in the continuum," Phys. Rev. Lett. **123**, 116104 (2019).
23. A. Chen, W. Liu, Y. Zhang, *et al.*, "Observing vortex polarization singularities at optical band degeneracies," Phys. Rev. B **99**, 180101 (2019).
24. X. Yin, J. Jin, M. Soljačić, *et al.*, "Observation of topologically enabled unidirectional guided resonances," Nature **580**, 467 (2020).
25. Y. Zeng, G. Hu, K. Liu, *et al.*, "Dynamics of topological polarization singularity in momentum space," Phys. Rev. Lett. **127**, 176101 (2021).
26. Y. Chen, H. Deng, X. Sha, *et al.*, "Observation of intrinsic chiral bound states in the continuum," Nature **613**, 474 (2023).
27. B. Wang, W. Liu, M. Zhao, *et al.*, "Generating optical vortex beams by momentum-space polarization vortices centred at bound states in the continuum," Nat. Photonics **14**, 623 (2020).
28. T. Yoda and M. Notomi, "Generation and annihilation of topologically protected bound states in the continuum and circularly polarized states by symmetry breaking," Phys. Rev. Lett. **125**, 053902 (2020).
29. X. Wang, J. Wang, X. Zhao, *et al.*, "Realizing tunable evolution of bound states in the continuum and circularly polarized points by symmetry breaking," ACS Photonics **10**, 2316 (2023).
30. K. Koshelev, P. Tonkaev, and Y. Kivshar, "Nonlinear chiral metaphotonics: a perspective," Adv. Photonics **5**, 064001 (2023).
31. W. Wang, A. Günzler, B. D. Wilts, *et al.*, "Unconventional bound states in the continuum from metamaterial-induced electron acoustic waves," Adv. Photonics **5**, 056005 (2023).
32. C. Han, J. He, C. Tong, *et al.*, "Generating first-order optical vortex beams by photonic crystal slabs," Opt. Express **32**, 27591 (2024).
33. S. Cai, J. Chen, X. Liu, *et al.*, "Perfect intrinsic and nonlinear chirality simultaneously driven by half-integer topological charge," Phys. Rev. B **109**, 165420 (2024).
34. M. Kang, S. Zhang, M. Xiao, *et al.*, "Merging bound states in the continuum at off-high symmetry points," Phys. Rev. Lett. **126**, 117402 (2021).
35. P. Hu, J. Wang, Q. Jiang, *et al.*, "Global phase diagram of bound states in the continuum," Optica **9**, 1353 (2022).
36. Q. Jiang, P. Hu, J. Wang, *et al.*, "General bound states in the continuum in momentum space," Phys. Rev. Lett. **131**, 013801 (2023).
37. S. Sharma, B. Lahiri, and S. Varshney, "Multispectral tunable symmetry-protected bound states in the continuum in all-dielectric split-ring resonator metasurfaces," J. Phys. D: Appl. Phys. **56**, 055104 (2023).
38. T. Li, J. Wang, W. Zhang, *et al.*, "High-efficiency nonlocal reflection-type vortex beam generation based on bound states in the continuum," National Sci. Rev. **10**, nwac234 (2023).
39. J. Wu, J. Chen, X. Qi, *et al.*, "Observation of accurately designed bound states in the continuum in momentum space," Photonics Res. **12**, 638 (2024).
40. J. Chen, J. Liu, F. Shu, *et al.*, "Merging of accidental bound states in the continuum in symmetry and symmetry-broken terahertz photonic crystal slabs," Nanomaterials **15**, 451 (2025).
41. J. Jin, X. Yin, L. Ni, *et al.*, "Topologically enabled ultrahigh-Q guided resonances robust to out-of-plane scattering," Nature **574**, 501 (2019).
42. H. Luo, L. Liu, Z. Xi, *et al.*, "Dynamics of diverse polarization singularities in momentum space with far-field interference," Phys. Rev. A **107**, 013504 (2023).